PHYSICAL REVIEW APPLIED **9,** 044021 (2018)

Designing Phononic Crystals with Wide and Robust Band Gaps

Zian Jia,[1] Yanyu Chen,[2] Haoxiang Yang,[1] and Lifeng Wang[1,*]
[1]*Department of Mechanical Engineering, State University of New York at Stony Brook,*
Stony Brook, New York 11794, USA
[2]*Transportation and Hydrogen Systems Center, National Renewable Energy Laboratory,*
Golden, Colorado 80401, USA

(Received 2 November 2017; revised manuscript received 31 January 2018; published 16 April 2018)

Phononic crystals (PnCs) engineered to manipulate and control the propagation of mechanical waves have enabled the design of a range of novel devices, such as waveguides, frequency modulators, and acoustic cloaks, for which wide and robust phononic band gaps are highly preferable. While numerous PnCs have been designed in recent decades, to the best of our knowledge, PnCs that possess simultaneous wide and robust band gaps (to randomness and deformations) have not yet been reported. Here, we demonstrate that by combining the band-gap formation mechanisms of Bragg scattering and local resonances (the latter one is dominating), PnCs with wide and robust phononic band gaps can be established. The robustness of the phononic band gaps are then discussed from two aspects: robustness to geometric randomness (manufacture defects) and robustness to deformations (mechanical stimuli). Analytical formulations further predict the optimal design parameters, and an uncertainty analysis quantifies the randomness effect of each designing parameter. Moreover, we show that the deformation robustness originates from a local resonance-dominant mechanism together with the suppression of structural instability. Importantly, the proposed PnCs require only a small number of layers of elements (three unit cells) to obtain broad, robust, and strong attenuation bands, which offer great potential in designing flexible and deformable phononic devices.

DOI: 10.1103/PhysRevApplied.9.044021

I. INTRODUCTION

Phononic crystals (PnCs) are architected materials that offer exceptional control over phonons, sound, and other mechanical waves [1]. In the architected material design, for example, periodical distribution of the density and/or elastic constants is capable of generating phononic band gaps, within which waves of certain frequencies cannot propagate through. Such a unique feature brings rich physical phenomena and enables a broad range of applications, including perfect mirrors [2], lenses [3,4], wave filters [5–7], waveguides [8–10], frequency modulators [11,12], acoustic cloaks [13–15], and thermal insulators [16,17].

To date, various structures have been designed and shown to possess complete band gaps. One early reported design is a type of periodic composite consisting of arrays of metal cylinders or spheres embedded in a polymer matrix [18]. By choosing materials with high mechanical impedance mismatch and adjusting the packing patterns, a maximum band-gap relative width (defined as the width of the band gap normalized by the middle gap frequency $\Delta\omega/\bar{\omega}$) of 70% is achieved [19]. Following a similar design strategy, more complex material structures are proposed using two-phase materials of high impedance contrast, such as 3D bicontinuous structures [20,21], brick-and-mortar structures [22,23], structures with additionally inserted cylinders [24,25], and structures with integrated local resonators [26–28]. On the other hand, numerical strategies such as topological optimization have been applied to optimize the band-gap width, which expands the relative band-gap width to around 100% [29–32]. However, the optimal structures either have too intricate interfacial shapes [30] or they have tiny geometric features [29], which are intrinsically geometry sensitive and pose a great challenge for manufacturability. Designing structures featuring a combination of wide band gaps and manufacturability is still challenging.

While the aforementioned designs are based on multiphase materials, single-phase material systems [33–35] have attracted attention more recently, as their monolithic structure can be fabricated more readily. By introducing architected porosity in solids, one can achieve complete band gaps, and in the meantime, reduce material weight. For instance, lattice materials with introduced chirality [36], self-similarity [37–39], crosslike holes [40,41], local curvature [42,43], and hierarchy [44] have been shown to open up band gaps or possess broader band gaps compared

---

[*] Corresponding author.
Lifeng.wang@stonybrook.edu

with conventional lattices. These designs give rise to band gaps by the redistribution of the constitutive material, which, in turn, changes the wave interaction within the material. Yet, structural features such as self-similarity or hierarchy themselves do not work as fundamental mechanisms of band-gap formation. The two broadly accepted physical mechanisms at the origin of phononic band gaps are Bragg scattering [45] and local resonances [26]. In the former case, a stronger wave velocity mismatch contributes to the formation of broader band gaps due to stronger wave scattering at the interfaces. However, phononic band gaps generated by Bragg scattering strongly depend on order and symmetry of the lattice as well as the shape of the scatters and are, thus, not robust. In the latter case, band gaps form due to localized excitation at the resonant frequencies, which are considered independent of periodicity [46], but the width of a local resonant gap is typically narrow [20,39,47]. That is why regardless of numerous PnCs proposed in recent decades [33–37,39,44], none have been shown to possess simultaneously wide and robust band gaps. Interestingly, recent studies have achieved PnCs with broader band gaps by combining these two mechanisms [20,48], which might provide one avenue of designing PnCs with simultaneously wide and robust band gaps.

Though structural periodicity and lattice symmetry are critical to the generation of phononic band gaps, studies show that interesting applications (e.g., acoustic switches) arise by breaking the original lattice symmetry with applied loads [49–51]. In addition to the tunability of the phononic crystals, in many applications (e.g., flexible phononic crystals), wide yet robust band gaps in regard to applied deformation or manufacturing defects are highly desirable. Very recently, topological metamaterials [52–55] have been shown to possess topologically protected band gaps that are robust against smooth deformations of the material. Such a remarkable feature has inspired much research in designing robust phononic crystals [55]. By contrast, nontopological materials are often considered sensitive to random changes in their microstructure [55]. Although PnCs with coated steel cylinders [46,56] and additional air cylinders [25] have demonstrated that it is also possible for nontopological materials to possess band gaps that are robust to geometric randomness, this topic remains largely unexplored.

In this work, we propose a type of PnC with artificially engineered geometric features. Specifically, a cylindrical mass is introduced to each cell wall of a conventional hexagonal lattice. Through a combination of numerical simulations and analytical formulations, we demonstrate the existence of simultaneously wide and robust band gaps in the proposed PnCs. This remarkable feature is attributed to the coexistence of Bragg scattering and local resonances, while the latter is dominant. The proposed design concept is also applicable to 3D PnCs exhibiting considerable band-gap width.

II. DESIGN OF 2D PHONONIC CRYSTALS

We begin by designing 2D PnCs with a hexagonal topology because high symmetry is typically essential to generate Bragg-type phononic band gaps. Since most 2D hexagonal phononic crystals exhibit only small partial band gaps [44], we artificially introduce concentrated masses (cylinders with relatively large diameter) at the center point of the hexagonal cell walls, aiming to achieve wide vibrational band gaps. Figure 1(a) shows a schematic of the designed 2D PnC, which is characterized by three geometric parameters: the hexagonal edge length a, the radius of the cylinder r, and the thickness of the ligament wall t.

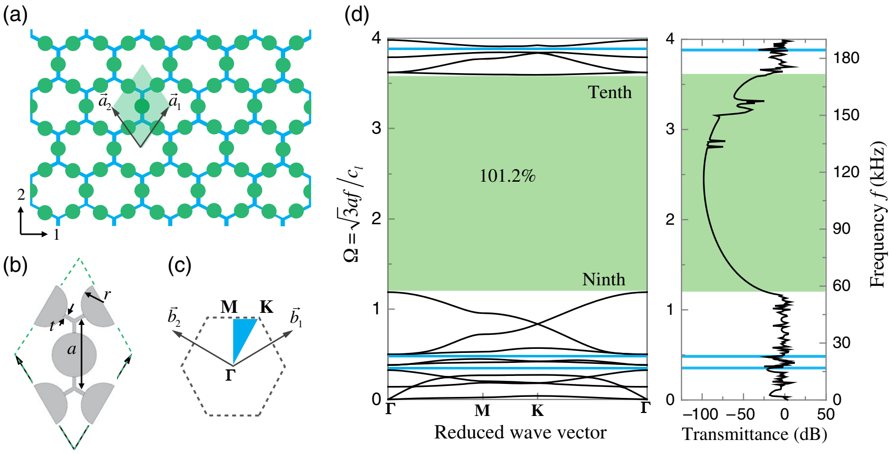

FIG. 1. Schematics and dispersion relation of the proposed 2D PnC. (a) The geometry of the 2D PnC with concentrated masses at the middle of each hexagonal edge. The unit cell is marked by the shaded region and magnified in plot (b), where t and a are the cell wall thickness and edge length of the basis honeycomb, respectively; r is the radius of the introduced cylinder. (c) The blue triangle shows the first irreducible Brillouin zone of the 2D PnC. $\vec{b}_1$, $\vec{b}_2$ are the reciprocal primitive vectors. (d) Dispersion relation and transmittance in the **Γ**-**M** direction of the 2D PnC with $r/a = 0.3$, $t/a = 0.05$, and $a = 5$ mm. The band gaps are marked by shaded areas, and the maximum band gap appears between the ninth and tenth bands with a relative width ($\Delta\omega/\bar{\omega}$) of 101.2%.

III. WIDE BAND GAPS IN 2D PHONONIC CRYSTALS

A. Numerical results

To study the propagation of small-amplitude elastic waves in the proposed 2D lattice, we perform eigenfrequency and frequency domain analyses with the finite-element method using the commercial software COMSOL Multiphysics. In brief, the phononic dispersion relation is obtained by solving the eigenfrequencies of the unit cell [Fig. 1(b)] with periodic boundary conditions described by the Bloch-Floquet theorem in the first irreducible Brillouin zone [Fig. 1(c)] [57]. Moreover, a frequency domain perturbation analysis is performed on finite-sized samples to obtain the transmittance [defined as the ratio between the output and input acceleration signals, $\|A_{\mathrm{out}}(f)/A_{\mathrm{in}}(f)\|$]. Quadratic triangular plain strain elements are used in the simulation, and the material is modeled as a linear elastic material with Young's modulus $E = 1750$ MPa, Poisson's ratio $\nu = 0.4$, and density $\rho = 930\ \mathrm{kg/m^3}$. Unless otherwise specified, the geometric parameters are taken as $r/a = 0.3$, $t/a = 0.05$ with edge length $a = 5$ mm [58].

Figure 1(d) shows the phononic dispersion relation and associated transmittance of a PnC with $r/a = 0.3$ and $t/a = 0.05$. Four complete band gaps are observed in the dispersion relation, with the maximum band gap appearing between the ninth and tenth modes. The maximum relative gap width ($\Delta\omega/\bar{\omega}$) is 101.2%, which is relatively wide compared with those reported in other honeycomb-based designs [36,37,44]. The transmittance calculated along the **Γ**-**M** direction drops approximately 90 dB in the frequency range $f = 56$–170 kHz, which matches perfectly with the band gaps in the dispersion relation. For comparison, we normalize the frequency by the equivalent longitudinal wave speed c_l (calculated from dispersion relation $c_l = \omega/k$) and lattice length of the unit cell as $\Omega = \sqrt{3}af/c_l$. The normalized frequency plotted in Fig. 1(d) shows that the ninth band is near normalized frequency of $\Omega = 1$, indicating a band-gap formation mechanism of Bragg scattering, as we discuss in Sec. III C.

The specimen sizes of the above phononic crystals are arbitrarily selected. We then examine the effect of geometric parameters on the evolution of the band gaps. Figures 2(a)–2(d) show the ninth and tenth Bloch modes at the high symmetric point of the Brillouin zone (**Γ**). Note that the tenth Bloch mode depends on the relative cylinder radius. Figures 2(e) and 2(f) show the evolution of the band gaps as the cell wall thickness t/a (r/a fixed at 0.3) and relative cylinder radius r/a (t/a fixed at 0.05) change, respectively. The results show that one wide band gap along with multiple relatively narrow band gaps exist for a wide range of geometric parameters, providing a relatively large design space of the proposed PnCs.

B. Analytical formulation and optimal design

To validate our numerical simulations and find optimal band gaps, theoretical models are proposed in this subsection to predict the frequencies of the band-gap edges. Figure 2(a) shows that the ninth mode can be simplified as lumped masses vibrating on springs. This mode is universal and controls the lower bounding frequencies for all geometric parameters considered in this paper. By contrast, three different modes exist for the tenth mode, depending on the cylinder radius. The mode at $r/a < 0.23$ is simplified as a 2D beam bending with one end pinned and the

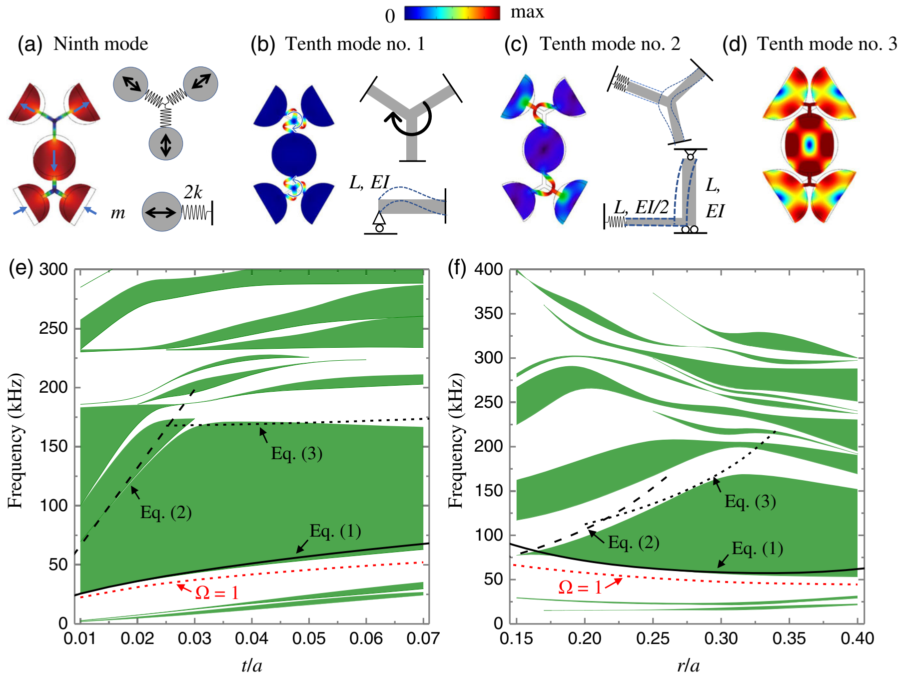

FIG. 2. Effect of geometric parameters on the band structure. Depending on the geometric parameters, one mode for the ninth Bloch mode (a) and three different modes for the tenth mode at (b) $r/a < 0.23$, (c) $0.23 < r/a < 0.33$, and (d) $r/a > 0.33$ are found. Plotted alongside is the theoretical modeling of these modes. (e) and (f) show the evolution of the band gaps as functions of t/a ($r/a = 0.3$) and r/a ($t/a = 0.05$). The green areas show the numerical results, the black lines show the eigenfrequencies calculated with Eqs. (1)–(3), and the red dashed lines show the location with normalized frequency $\Omega = 1$. E is the Young's modulus of the constituent and I is the moment of inertia.

other end fixed [Fig. 2(b)]. For $0.23 < r/a < 0.33$, the mode is characterized by a truss-beam system vibrating on an elastic support [Fig. 2(c)], while for larger radius $r/a > 0.33$, the mode shape is controlled by the in-plane deformation of cylinders [Fig. 2(d)]. Using structural mechanics formulations [59,60], we derive the corresponding bounding eigenfrequencies as [58]

$$f_{\mathrm{ninth}} = \frac{1}{2\pi}\sqrt{\frac{4Et}{\rho\pi r^2(a-2r)}}, \qquad (1)$$

$$f_{\mathrm{tenth}}^{1} = \frac{1}{2\pi}\left(\frac{60.672}{(a-2r)^2}\right)\sqrt{\frac{Et^2}{12\rho}}, \qquad (2)$$

$$f_{\mathrm{tenth}}^{2} = \frac{1}{2\pi}\left(\frac{1}{(a-2r)^2}\right)\sqrt{\frac{\pi^4 Et^2 + 48CE(a-2r)^2}{16\rho}}, \qquad (3)$$

where f_{ninth} is the ninth mode frequency, f_{tenth}^{1} and f_{tenth}^{2} are the tenth mode frequencies for $r/a < 0.23$ and $0.23 < r/a < 0.33$, respectively, E and ρ are Young's modulus and the density of the constituent material, and $C \approx 0.78$ is the end constraint factor of the elastic support obtained by comparing with numerical results. The band-gap location predicted with Eqs. (1)–(3) is plotted in Figs. 2(e) and 2(f) as a function of r/a (t/a fixed at 0.05) and t/a (r/a fixed at 0.3). Compared with the numerical results, the theoretical equations exhibit excellent accuracy.

Moreover, the analytical models can be used to find the optimal geometric parameters of the PnCs with a maximum band gap. Figure 3(a) shows the relative band-gap width between the ninth and tenth bands as a function of r/a and t/a calculated theoretically with $\Delta\omega/\bar{\omega} = 2(f_{\mathrm{tenth}} - f_{\mathrm{ninth}})/(f_{\mathrm{tenth}} + f_{\mathrm{ninth}})$. The map shows that the band gap opens at $r/a = 0.15$ and increases with r/a. Interestingly, there exists an optimal cell wall thickness given a cylinder radius, which is marked by the dashed line in Fig. 3(a). With this map, a maximum relative band-gap width of 126.94% is predicted at $t/a = 0.03$ and $r/a = 0.33$. The dispersion relation of this optimal geometry is numerically calculated, as shown in Fig. 3(b), where a relative gap width of 119.28% is observed. Note that the theoretical estimation is applied only to the range of $r/a < 0.33$ because eigenfrequencies outside this range are controlled by the cylinder deformation [Fig. 2(d)], for which an explicit expression is not yet available. Notably, the gap width starts to decrease when the cylinder in-plane deformation becomes dominant [verified in Fig. 2(g)]. Figure 3(c) shows a PnC with relatively narrow cell wall ($t/a = 0.02$ and $r/a = 0.33$), which has quite a different dispersion relation compared to Fig. 3(b). With a narrow cell wall, an extra band gap opens between the 10th and 11th band next to the original one, and these two side-by-side gaps give a total relative width of 128.96%.

C. Band-gap formation mechanisms

In this section, we discuss the mechanism of forming wide band gaps. In the previous section, we show that the cylinders vibrate in the ninth mode with the narrow connectors acting as springs, while in the tenth mode, the cell walls vibrate with the cylinders nearly at rest. As a result, the vibration energy is localized in the local modes, preventing the propagation of the elastic waves. This is verified by the accuracy of Eqs. (1)–(3) in predicting the maximum band-gap locations. For this reason, local resonances are commonly considered as the band-gap formation mechanism of systems composed of large lumps and narrow connectors, as reported in Refs. [32,40,41].

However, the dispersion relation of the proposed PnC shown in Fig. 1(d) does not match that of PnCs with purely

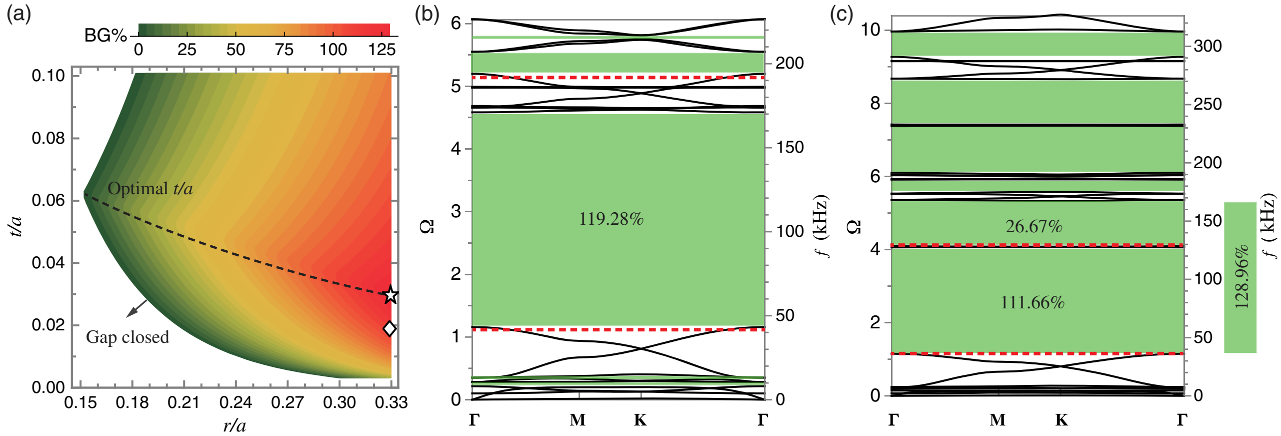

FIG. 3. (a) Theoretical prediction of the relative gap width between the ninth and tenth bands. The dashed line shows the optimal relative cell wall thickness t/a at a given relative cylinder radius r/a. The dispersion relations of the star (PnC with theoretically predicted maximum band-gap width at $t/a = 0.03$ and $r/a = 0.33$) and diamond (PnC with relatively thin cell wall thickness $t/a = 0.02$ and $r/a = 0.33$) shown in (a) are calculated numerically and the results are shown in (b) and (c), respectively. Theoretical predictions are marked by red dashed lines.

local resonant band gaps [26,27,47,61]. Several key differences can be distinguished. First, the band edges are flat for purely local resonant PnCs, corresponding to zero group velocities [20], while the lower edge of the proposed PnCs shows clear valleys. Second, purely local resonant band gaps are typically narrow (<20%) even with strong impedance mismatch [26,49], while the band gap of the proposed PnC is very wide (>100%). Third, purely local resonant band gaps are often formed at the subwavelength scale [47]. These observations suggest that the band gaps of the proposed PnCs are not produced purely by local resonances. The fact that the proposed PnC band gap is near a normalized frequency of $\Omega = 1$ suggests that the band gap might be related to the overlapping of local resonances and Bragg scattering, which has been reported in Refs. [20,48]. To further verify this, we plot the $\Omega = 1$ curve in the parametric map of the band gap as functions of r/a and t/a, respectively [red dashed lines in Figs. 2(e) and 2(f)]. The results clearly show that the lower edge of the maximum band gap intimately follows the curves of $\Omega = 1$. This behavior of the band gap is strong evidence that Bragg scattering also controls the lower edge of the maximum band gap (but not the upper one).

Combining the above arguments, we conclude that both local resonances and Bragg scattering contribute to the band-gap formation of the proposed PnC (overlapping). More specifically, local resonances affect both the upper edge and the lower edge of the band gap, while Bragg scattering affects only the lower edge, suggesting that local resonances are the dominant mechanism. This overlapping of local resonances and Bragg scattering is the fundamental reason for the observed wide band gaps and form the basis of designing wide and robust PnCs.

IV. BAND-GAP ROBUSTNESS IN 2D PHONONIC CRYSTALS

In practical applications, defects in the PnC geometry, like inaccurate sizes and misalignments, cannot be avoided in the manufacturing process. These unexpected imperfections can potentially affect the operational frequency ranges of the PnCs. In addition, PnCs might also be deployed in applications where external stimuli cannot be avoided, such as on the surface of submarines and in vibrational conditions, where external load-induced deformations will arise. Moreover, flexible phononic crystal designs require stable wave attenuation ability at moderate deformations. These challenges motivate us to further examine the robustness of the wide band gaps to both geometric randomness and deformations.

A. Robustness to geometric randomness

In all previous reports on the effect of randomness on phononic crystals [26,46,56], only the distribution of local resonators is considered random, while each resonator is assumed to have ideal geometry and no randomness (so the resonant frequency is not affected at all). Here, we perform a more extensive and rigorous examination of the effect of randomness on PnCs, where all geometric parameters are assumed to be random, including the cell wall thickness t, cylinder radius r, and hexagonal node locations. These parameters are assumed to follow normal distributions, and the intensity of randomness is controlled by the standard deviation (STD) or relative standard deviation (RSD defined as STD divided by the average value). The perturbation added to each node is a displacement vector $\vec{\mathbf{N}}$ described by its amplitude $|\vec{\mathbf{N}}|$ (follows a normal distribution) and direction angle (follows uniform distribution) [58]. Figure 4(a) shows one perturbed PnC generated using this method, with average geometric parameter $a_0 = 5$ mm, $t_0 = 0.05a_0$, $r_0 = 0.3a_0$, and random intensity characterized by STD of t as $s_t = 0.1t_0$, r as $s_r = 0.1r_0$, and $|\vec{\mathbf{N}}|$ as $s_{|\vec{\mathbf{N}}|} = 0.1a_0$ (10% RSD of all parameters). The effect of randomness on the band gap is then evaluated by comparing the wave transmittance curves of the unperturbed structure and three perturbed structures as shown in Fig. 4(b). The results show that strong wave attenuation is maintained within the band gap even at 10% RSD of t, r, and $|\vec{\mathbf{N}}|$. To clarify this, we plot the dynamic response of the PnC with and without perturbations in Fig. 4(c). The dynamic displacement fields show that at a frequency of 50 kHz (outside of the band gap) waves are transmitted regardless of the existence of randomness, while at a frequency of 100 kHz (inside the band gap), the excitation is localized because there is no transmission mode. It is worth noting that the dynamic response of the perturbed structure is not symmetric because of the randomness, and only the longitudinal wave transmittance in direction 2 is demonstrated because either transverse wave or propagation in direction 1 gives similar results [58]. More simulations of randomness provided in Ref. [58] show that the attenuation is similarly retained with the individual perturbation of t, r, and $\vec{\mathbf{N}}$, and with 15% RSD of combined t, r, and $|\vec{\mathbf{N}}|$, which strongly proves the robustness of the PnC towards possible geometric randomness.

Furthermore, one noticeable feature in Fig. 4(b) is that randomness tends to have a more significant influence on the upper bound than the lower one. To obtain a quantitative description of this observation, we apply an uncertainty analysis on the bounding frequencies of the band gap. The effect of geometric randomness is modeled by propagation of uncertainty from t, r, a toward band frequencies f_{ninth} and f_{tenth} through Eqs. (1)–(3). Using the variance formula [62], the RSDs of the bounding frequencies are derived as [58]

$$f_{\text{ninth}}^{\text{RSD}} = \sqrt{\frac{1}{4}t_{\text{RSD}}^2 + \left(\frac{1-3\bar{r}}{1-2\bar{r}}\right)^2 r_{\text{RSD}}^2 + \frac{1}{4(1-2\bar{r})^2}a_{\text{RSD}}^2}, \qquad (4)$$

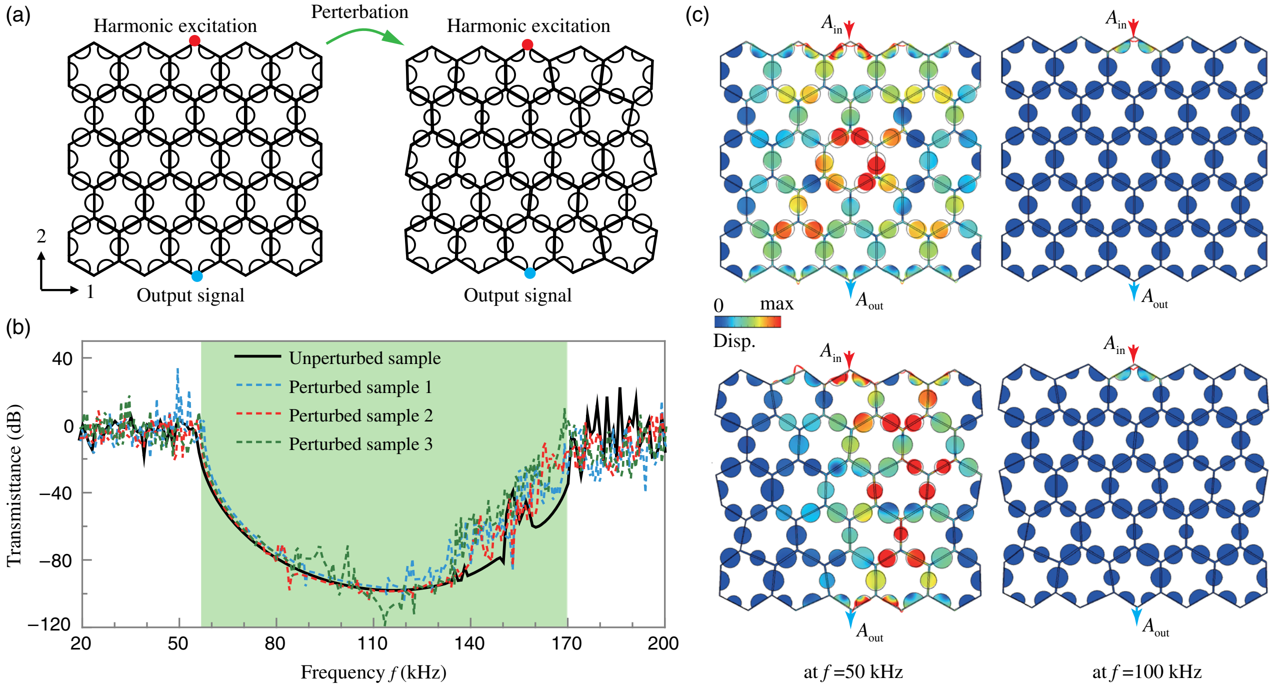

FIG. 4. Effect of geometric randomness on the transmittance. (a) The left shows the unperturbed sample with 5 × 5 unit cells of size $t/a = 0.05$, $r/a = 0.3$, $a = 5$ mm, and the right shows the sample with perturbation levels of $s_t = 0.1t_0$, $s_r = 0.1r_0$, $s_{|\vec{\mathbf{N}}|} = 0.1a_0$. (b) Comparison of the transmittance between the unperturbed sample and three perturbed samples; the shaded area shows the band gap of the unperturbed PnC. Note only longitudinal waves transmitting in direction 2 are shown for simplicity. (c) Displacement fields of the unperturbed (top) and perturbed (bottom) structure at frequencies of 50 kHz (left) and 100 kHz (right). The deformations are magnified properly for easy viewing.

$$f^{\rm RSD}_{{\rm tenth},1} = \sqrt{t^2_{\rm RSD} + \frac{16}{(1/\bar{r}-2)^2} r^2_{\rm RSD} + \frac{4}{(1-2\bar{r})^2} a^2_{\rm RSD}}, \tag{5}$$

$$f^{\rm RSD}_{{\rm tenth},2} = \sqrt{\left(\frac{\pi^4\bar{t}^2}{2\bar{t}^2_*}\right)^2 t^2_{\rm RSD} + \left(\frac{4-96C(1-2\bar{r})^2/\bar{t}^2_*}{1/\bar{r}-2}\right)^2 r^2_{\rm RSD} + \left(\frac{2-48C(1-2\bar{r})^2/\bar{t}^2_*}{1-2\bar{r}}\right)^2 a^2_{\rm RSD}}, \tag{6}$$

where $f^{\rm RSD}$, $t_{\rm RSD}$, $r_{\rm RSD}$, and $a_{\rm RSD}$ denote the relative standard deviations of the frequency, cell wall thickness, cylinder radius, and honeycomb edge length, respectively, $\bar{t} = t/a$ and $\bar{r} = r/a$ are the relative thickness and radius, respectively, and $\bar{t}_* = \sqrt{\pi^2\bar{t}^2 + 36C(1-2\bar{r})^2}$ is the equivalent relative thickness. Using the parameters of $\bar{r} = 0.3$, $\bar{t} = 0.05$, we have

$$f^{\rm RSD}_{\rm ninth} = \sqrt{0.25t^2_{\rm RSD} + 0.0625r^2_{\rm RSD} + 0.625a^2_{\rm RSD}} \quad \text{and}$$
$$f^{\rm RSD}_{{\rm tenth},2} = \sqrt{3.63\times 10^{-3}t^2_{\rm RSD} + 2.42r^2_{\rm RSD} + 6.73a^2_{\rm RSD}}. \tag{7}$$

For 10% geometric RSD ($t_{\rm RSD} = r_{\rm RSD} = a_{\rm RSD} = 0.1$), we calculate $f^{\rm RSD}_{\rm ninth} = 0.0968$ and $f^{\rm RSD}_{{\rm tenth},2} = 0.303$, which shows that the RSD of the upper bounding frequency is magnified approximately 3 times, while RSD of the lower bounding frequency stays at the same level. This calculation explains why a stronger fluctuation is exhibited near the tenth band in the transmittance curve, while the ninth band is more stable under the same level of perturbation. Furthermore, Eqs. (4)–(6) also give quantitative results of how the randomness of the node location, cylinder radius, and cell wall thickness affect the band gap, giving suggestions of which parameters are of major concern in manufacturing. For instance, Eq. (7) shows that the thickness has a negligible influence on the maximum band gap, which is consistent with the results provided in the Supplemental Material [58], Fig. S6.

B. Robustness to deformation

In addition to the break of order and symmetry induced by geometric randomness, PnCs might also be subject to structural loads, which can induce certain deformations. Here we examine the band-gap properties of the deformed

PnCs, including uniaxial compression and simple shear deformation. Mechanical deformations are calculated prior to the wave transmission analysis by solving the stationary equilibrium equation and compatibility equation of solid mechanics with COMSOL MULTIPHYSICS. The compression and simple shear boundary conditions are applied with prescribed displacements that follow the periodic deformation condition [58,63,64]. It is worth noting that one remarkable feature of the proposed PnC is that a thickness of three elements gives wave attenuation over 60 dB within the band gap (Fig. S5 in Ref. [58]) similar to an early report [26]. For this reason, as well as to reduce the amount of computation, we demonstrate the effect of deformation on transmittance with a sample of 3 × 3 unit cells. Figure 5 shows the transmittance of an unperturbed PnC and that are under compression ($\varepsilon_1 = -0.2$ and $\varepsilon_2 = -0.2$) and simple shear ($\gamma_{12} = 0.2$). We find that the transmittance of the PnC under deformations exhibits similar attenuation compared with the PnC without deformation, quite different from the previously reported PnCs whose band gap closed after compression [27]. The wave attenuation ability is retained because the geometric pattern of the proposed structure is not changed after applying deformations, unlike the pattern transformation induced by instability [27,50]. For example, the original honeycomb exhibits a buckling mode when compressed in direction 2 [65]; however, this mode is suppressed by the existence of cylinders in the proposed PnC. As such, each individual element works effectively as sites of local resonances, and the PnC shows strong deformation robustness.

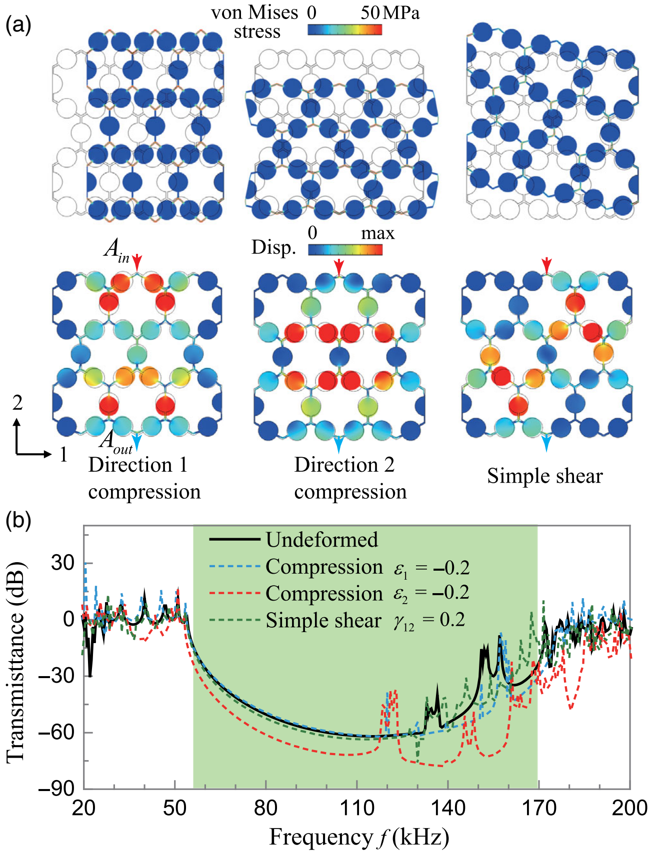

FIG. 5. Effect of deformation on the transmittance. (a) The first row shows the static stress field of an unperturbed sample with 3 × 3 unit cells under compression in direction 1 $\varepsilon_1 = -0.2$ (left), direction 2 $\varepsilon_2 = -0.2$ (middle), and simple shear $\gamma_{12} = 0.2$ (right). The second row shows the dynamic perturbation field of displacement under harmonic excitation at $f = 50$ kHz (in material coordinate). (b) Transmittance comparison (longitudinal waves) between the undeformed and deformed samples. The band gap of the undeformed PnC is highlighted by the green area.

C. Robustness to combined randomness and deformation

So far, the effect of randomness and deformation are considered separately, while in reality, these two factors can

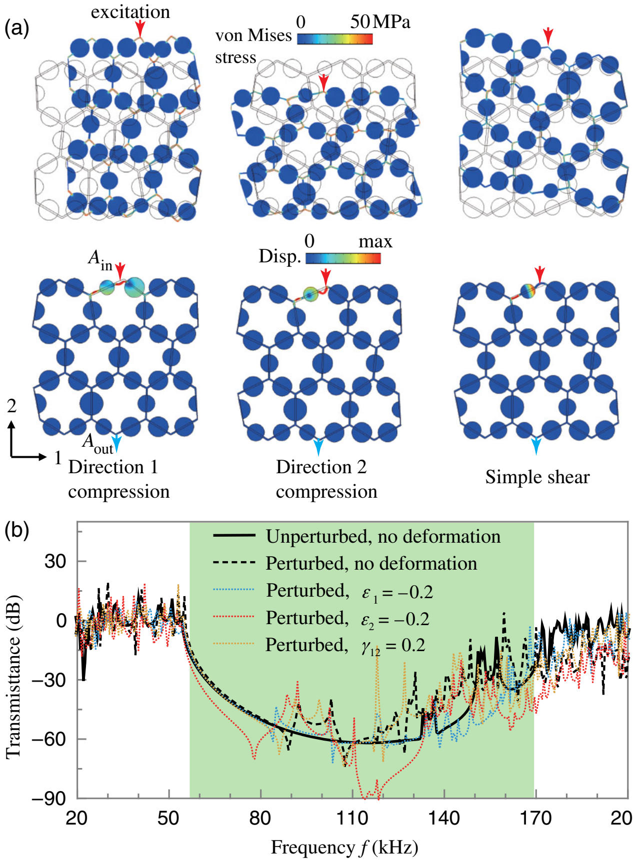

FIG. 6. Combined effect of deformation and randomness. The perturbed sample (3 × 3 unit cells) is generated with $t/a = 0.05$, $r/a = 0.3$, $a = 5$ mm, and randomness intensity 10% RSD of t, r, and $|\vec{\mathbf{N}}|$. (a) The top row shows the static stress field of the perturbed sample under compression with $\varepsilon_1 = -0.2$ (left), $\varepsilon_2 = -0.2$ (middle), and simple shear $\gamma_{12} = 0.2$ (right). The second row shows the dynamic displacement field under harmonic excitation at $f = 100$ kHz (in material coordinate). (b) Transmittance comparison (longitudinal waves) between the unperturbed sample with no deformation, perturbed sample with no deformation, and perturbed samples with applied deformations. The green area highlights the original phononic band gap.

simultaneously take place. Therefore, we further investigate the coupled effect of randomness and deformation by comparing the transmittance of a PnC with introduced randomness (10% RSD of t, r, and $|\vec{\mathbf{N}}|$) under compressive ($\varepsilon_1 = -0.2$, $\varepsilon_2 = -0.2$) and simple shear ($\gamma_{12} = 0.2$) loads. Figure 6(a) shows the static stress field under deformation and the dynamic displacement field at an input harmonic excitation of 100 kHz. The deformation is not as homogeneous as that for an unperturbed structure [Fig. 5(a)] due to structure randomness. But still, no pattern transformation is observed under combined randomness and deformations. As a result, the transmittance curves in Fig. 6(b) show strong attenuation within the band-gap region, demonstrating the super robustness of the PnC even with only three layers of unit cells.

In addition, the current PnC is designed on a hexagonal lattice basis, and it is worth pointing out that there are various 2D lattice structures to build on, e.g., triangular lattices and kagome lattices [66]. Such a broad range of choices provides a wide design space of the proposed designing methodology from which PnCs with wide and robust band gaps can be envisioned.

V. DESIGN CONCEPT EXTENDED TO 3D

While all the discussions so far are for 2D periodic materials, we now demonstrate that similar designs can be extended to 3D structures with various packing patterns. The 3D PnCs are designed based on spheres packed in simple-cubic (sc), body-centered-cubic (bcc), and face-centered-cubic (fcc) lattices, with the nearest spheres connected by ligaments [Fig. 7(a)]. Because geometric roundup between the ligaments and spheres is mechanically more preferable and is typically found in manufactured structures (e.g., lithography [67]), smooth connections between the spheres are assumed. As such, the ligaments are constructed by revolving arcs that tangentially connect two spheres, which is totally defined by the minimum diameter d and length h. As a demonstration, we generate three PnCs with sc lattice, bcc lattice, and fcc lattice [68]. Here, the geometric parameters are fixed at $d = 0.3r$ and $h = 0.5r$. The resultant 3D unit cells and corresponding irreducible Brillouin zone can be found in Ref. [58]. Figures 7(b)–7(d) show the simulated dispersion relations revealing that the sc PnC exhibits the widest relative gap width of 100.03%, followed by an 86.87% relative width of the bcc PnC, and 70.31%

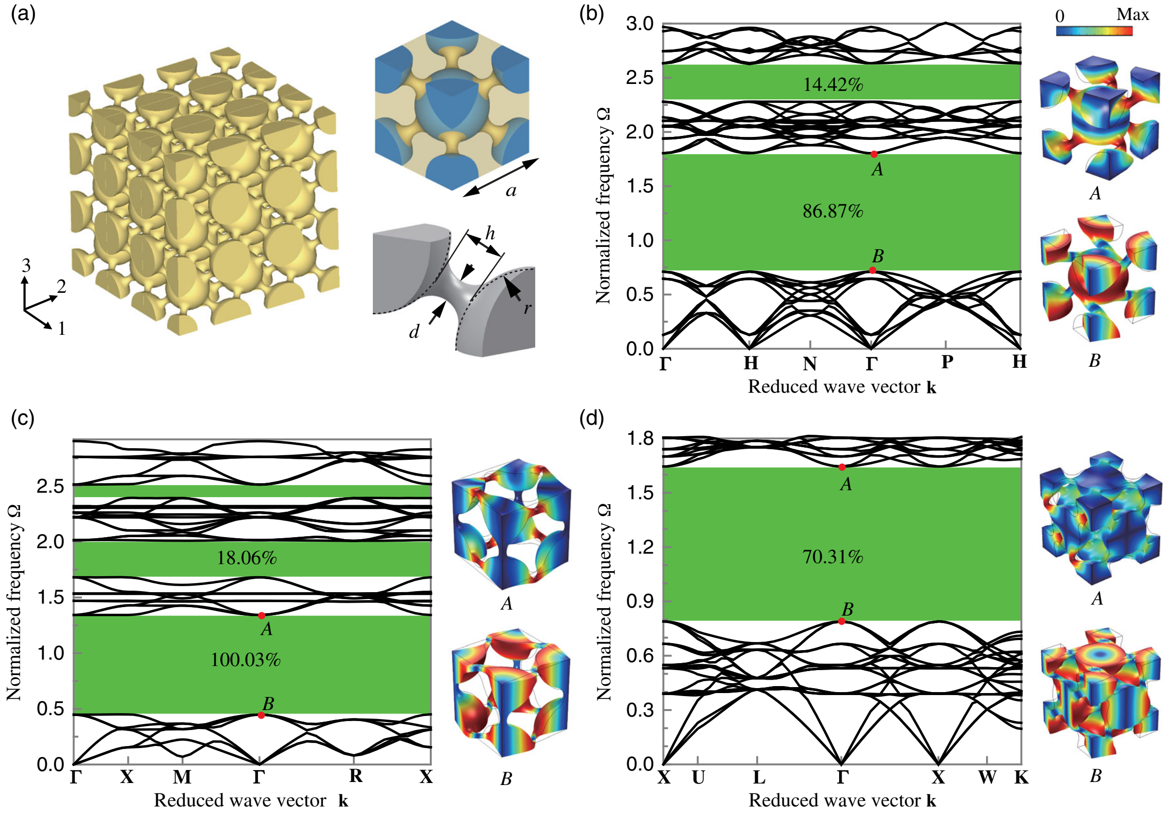

FIG. 7. Design concept extended to 3D PnCs. (a) The left shows a sample of a 3D PnC with bcc symmetry. The upper right shows the unit cell of the sample, where blue spheres are connected by yellow ligaments. The ligaments are generated by revolving arcs tangentially connecting the spheres for smooth geometry (bottom right). The 3D geometries are defined by the minimum ligament diameter d, ligament height h, and sphere radius r. (b)–(d) show the dispersion relations for the PnCs with bcc, sc, and fcc symmetry and $d = 0.3r$ and $h = 0.5r$. On the right of each figure the Bloch mode is shown at $\mathbf{\Gamma}$ of the upper (point A) and lower boundary (point B) of the maximum band gaps.

relative width of the fcc PnC. Like the 2D PnC, all the 3D PnCs show wide band gaps around normalized frequency $\Omega = 1$, indicating an overlapping of the Bragg-type band gap and local resonant band gap. One difference of the 3D PnCs compared with 2D PnCs is the higher connectivity between the spheres. For example, each sphere in the sc lattice is connected to six nearest spheres, corresponding to a coordinate number $Z = 6$. The coordinate numbers for the bcc lattice and fcc lattice are 8 and 12, respectively. We notice that the Bloch modes of the 3D PnCs are strongly dependent on the coordinate number, which is intrinsically dedicated to the connecting stiffness. Interestingly, all the lower bounding modes of the proposed 3D PnCs are in-plane rotations of the spheres [Figs. 7(b)–7(d)]. By contrast, the upper bounding modes are more complex; one observation is that all the modes are antisymmetric. This observation indicates that the eigenfrequency difference between symmetric modes and antisymmetric modes gives rise to the wide band gaps of the 3D PnCs (see Fig. S9 in the Supplemental Material [58]).

The current results show the existence of wide band gaps in 3D PnCs. Since their geometries are analogous to the 2D structure and they share the same gap formation mechanism, we, thus, may expect similar robustness in the 3D PnCs (i.e., ligament buckling should be suppressed to perform deformation robustness). In addition, although one phase material is assumed in our design, the fabrication methods allow the simultaneous fabrication of multiphase materials (e.g., 3D printing). With multiphase materials techniques, the ligaments can be replaced with softer materials, which are capable of further extending the band-gap width as reported in Ref. [69].

VI. CONCLUSIONS

In summary, we design a class of single-phase lightweight PnCs by introducing cylindrical or spherical masses on lattice structures and demonstrate the simultaneous wideness and robustness of the produced band gaps. While previous research suggests that the wide band gaps of lump, narrow connector systems are formed purely from local resonances, we give strong evidence that Bragg scattering also plays an important role, revealing the band-gap formation mechanism as overlapping Bragg scattering and local resonances. The analytical formulations derived from structural mechanics accurately predict the band-gap location and give the optimal design of the 2D PnC with the maximum band gap.

Robustness of manufacturing defects and deformations are considered in this work for future industrial applications of PnCs. In studying the manufacturing defect robustness, quantitative results of the randomness effect on PnC band gaps with an uncertainty analysis are obtained. Using numerical simulations, we show that the band gaps of the proposed PnCs are robust toward random perturbations, applied deformations, and a coupling of these two factors. Importantly, we show the deformation robustness originates from the local resonance dominant mechanism combined with the suppression of structure instability by the introduced cylinders. For porous PnCs, a local resonant mechanism alone does not guarantee a deformation robust band gap. The findings reported here provide not only a routine to design lightweight PnCs with wide and robust band gaps, but they also offer a wide range of potential applications such as thin-layer materials for noise and vibration control, robust devices for wave modulation and mitigation, and flexible or deformable phononic devices.

ACKNOWLEDGMENTS

The authors gratefully acknowledge the support from the National Science Foundation (Grant No. CMMI-1462270) and the Office of Naval Research (Dr. Yapa Rajapakse, Solid Mechanics Program).

[1] T. Gorishnyy, M. Maldovan, C. Ullal, and E. Thomas, Sound ideas, Phys. World **18**, 24 (2005).

[2] A. Khelif, B. Djafari-Rouhani, J. Vasseur, and P. Deymier, Transmission and dispersion relations of perfect and defect-containing waveguide structures in phononic band gap materials, Phys. Rev. B **68**, 024302 (2003).

[3] S. Yang, J. H. Page, Z. Liu, M. L. Cowan, C. T. Chan, and P. Sheng, Focusing of Sound in a 3D Phononic Crystal, Phys. Rev. Lett. **93**, 024301 (2004).

[4] J. Zhu, J. Christensen, J. Jung, L. Martin-Moreno, X. Yin, L. Fok, X. Zhang, and F. Garcia-Vidal, A holey-structured metamaterial for acoustic deep-subwavelength imaging, Nat. Phys. **7**, 52 (2011).

[5] T. Elnady, A. Elsabbagh, W. Akl, O. Mohamady, V. Garcia-Chocano, D. Torrent, F. Cervera, and J. Sánchez-Dehesa, Quenching of acoustic bandgaps by flow noise, Appl. Phys. Lett. **94**, 134104 (2009).

[6] K. M. Ho, C. K. Cheng, Z. Yang, X. Zhang, and P. Sheng, Broadband locally resonant sonic shields, Appl. Phys. Lett. **83**, 5566 (2003).

[7] M. Sigalas, Defect states of acoustic waves in a two-dimensional lattice of solid cylinders, J. Appl. Phys. **84**, 3026 (1998).

[8] A. Khelif, A. Choujaa, S. Benchabane, B. Djafari-Rouhani, and V. Laude, Guiding and bending of acoustic waves in highly confined phononic crystal waveguides, Appl. Phys. Lett. **84**, 4400 (2004).

[9] J. Vasseur, A.-C. Hladky-Hennion, B. Djafari-Rouhani, F. Duval, B. Dubus, Y. Pennec, and P. Deymier, Waveguiding in two-dimensional piezoelectric phononic crystal plates, J. Appl. Phys. **101**, 114904 (2007).

[10] Z. Tian and L. Yu, Rainbow trapping of ultrasonic guided waves in chirped phononic crystal plates, Sci. Rep. **7**, 40004 (2017).

[11] M. Kafesaki, M. Sigalas, and N. Garcia, Frequency Modulation in the Transmittivity of Wave Guides in Elastic-Wave Band-Gap Materials, Phys. Rev. Lett. **85**, 4044 (2000).

[12] W. Cheng, J. Wang, U. Jonas, G. Fytas, and N. Stefanou, Observation and tuning of hypersonic bandgaps in colloidal crystals, Nat. Mater. **5**, 830 (2006).

[13] R. Fleury, F. Monticone, and A. Alù, Invisibility and Cloaking: Origins, Present, and Future Perspectives, Phys. Rev. Applied **4**, 037001 (2015).

[14] S. A. Cummer and D. Schurig, One path to acoustic cloaking, New J. Phys. **9**, 45 (2007).

[15] X. Zhu, B. Liang, W. Kan, X. Zou, and J. Cheng, Acoustic Cloaking by a Superlens with Single-Negative Materials, Phys. Rev. Lett. **106**, 014301 (2011).

[16] M. Maldovan, Sound and heat revolutions in phononics, Nature (London) **503**, 209 (2013).

[17] P. E. Hopkins, C. M. Reinke, M. F. Su, R. H. Olsson III, E. A. Shaner, Z. C. Leseman, J. R. Serrano, L. M. Phinney, and I. El-Kady, Reduction in the thermal conductivity of single crystalline silicon by phononic crystal patterning, Nano Lett. **11**, 107 (2011).

[18] M. S. Kushwaha, P. Halevi, L. Dobrzynski, and B. Djafari-Rouhani, Acoustic Band Structure of Periodic Elastic Composites, Phys. Rev. Lett. **71**, 2022 (1993).

[19] J. Vasseur, P. Deymier, B. Chenni, B. Djafari-Rouhani, L. Dobrzynski, and D. Prevost, Experimental and Theoretical Evidence for the Existence of Absolute Acoustic Band Gaps in Two-Dimensional Solid Phononic Crystals, Phys. Rev. Lett. **86**, 3012 (2001).

[20] Y. Chen and L. Wang, Periodic co-continuous acoustic metamaterials with overlapping locally resonant and Bragg band gaps, Appl. Phys. Lett. **105**, 191907 (2014).

[21] Y. Chen, H. Yao, and L. Wang, Acoustic band gaps of three-dimensional periodic polymer cellular solids with cubic symmetry, J. Appl. Phys. **114**, 043521 (2013).

[22] Y. Chen and L. Wang, Multiband wave filtering and waveguiding in bio-inspired hierarchical composites, Extreme Mech. Lett. **5**, 18 (2015).

[23] Y. Chen and L. Wang, Tunable band gaps in bio-inspired periodic composites with nacre-like microstructure, J. Appl. Phys. **116**, 063506 (2014).

[24] Y. Lai, X. Zhang, and Z.-Q. Zhang, Engineering acoustic band gaps, Appl. Phys. Lett. **79**, 3224 (2001).

[25] Y. Lai and Z.-Q. Zhang, Large band gaps in elastic phononic crystals with air inclusions, Appl. Phys. Lett. **83**, 3900 (2003).

[26] Z. Liu, X. Zhang, Y. Mao, Y. Zhu, Z. Yang, C. T. Chan, and P. Sheng, Locally resonant sonic materials, Science **289**, 1734 (2000).

[27] P. Wang, F. Casadei, S. Shan, J. C. Weaver, and K. Bertoldi, Harnessing Buckling to Design Tunable Locally Resonant Acoustic Metamaterials, Phys. Rev. Lett. **113**, 014301 (2014).

[28] S. Zhang, J. Hui Wu, and Z. Hu, Low-frequency locally resonant band-gaps in phononic crystal plates with periodic spiral resonators, J. Appl. Phys. **113**, 163511 (2013).

[29] O. R. Bilal and M. I. Hussein, Ultrawide phononic band gap for combined in-plane and out-of-plane waves, Phys. Rev. E **84**, 065701 (2011).

[30] H.-W. Dong, X.-X. Su, Y.-S. Wang, and C. Zhang, Topological optimization of two-dimensional phononic crystals based on the finite element method and genetic algorithm, Struct. Multidiscip. Optim. **50**, 593 (2014).

[31] Y. Lu, Y. Yang, J. K. Guest, and A. Srivastava, 3-D phononic crystals with ultra-wide band gaps, Sci. Rep. **7**, 43407 (2017).

[32] H.-W. Dong, Y.-S. Wang, Y.-F. Wang, and C. Zhang, Reducing symmetry in topology optimization of two-dimensional porous phononic crystals, AIP Adv. **5**, 117149 (2015).

[33] A. H. Safavi-Naeini, J. T. Hill, S. Meenehan, J. Chan, S. Gröblacher, and O. Painter, Two-Dimensional Phononic-Photonic Band Gap Optomechanical Crystal Cavity, Phys. Rev. Lett. **112**, 153603 (2014).

[34] F. Javid, P. Wang, A. Shanian, and K. Bertoldi, Architected materials with ultra-low porosity for vibration control, Adv. Mater. **28**, 5943 (2016).

[35] M. D. Guild, V. M. García-Chocano, J. Sánchez-Dehesa, T. P. Martin, D. C. Calvo, and G. J. Orris, Aerogel as a Soft Acoustic Metamaterial for Airborne Sound, Phys. Rev. Applied **5**, 034012 (2016).

[36] A. Spadoni, M. Ruzzene, S. Gonella, and F. Scarpa, Phononic properties of hexagonal chiral lattices, Wave Motion **46**, 435 (2009).

[37] D. Mousanezhad, S. Babaee, R. Ghosh, E. Mahdi, K. Bertoldi, and A. Vaziri, Honeycomb phononic crystals with self-similar hierarchy, Phys. Rev. B **92**, 104304 (2015).

[38] Y. Tang, G. Lin, L. Han, S. Qiu, S. Yang, and J. Yin, Design of hierarchically cut hinges for highly stretchable and reconfigurable metamaterials with enhanced strength, Adv. Mater. **27**, 7181 (2015).

[39] N.-K. Kuo and G. Piazza, Fractal phononic crystals in aluminum nitride: An approach to ultra high frequency bandgaps, Appl. Phys. Lett. **99**, 163501 (2011).

[40] Y.-F. Wang, Y.-S. Wang, and X.-X. Su, Large bandgaps of two-dimensional phononic crystals with cross-like holes, J. Appl. Phys. **110**, 113520 (2011).

[41] Y.-F. Wang and Y.-S. Wang, Multiple wide complete bandgaps of two-dimensional phononic crystal slabs with cross-like holes, J. Sound Vib. **332**, 2019 (2013).

[42] G. Trainiti, J. Rimoli, and M. Ruzzene, Wave propagation in periodically undulated beams and plates, Int. J. Solids Struct. **75**, 260 (2015).

[43] G. Trainiti, J. J. Rimoli, and M. Ruzzene, Wave propagation in undulated structural lattices, Int. J. Solids Struct. **97**, 431 (2016).

[44] Y. Chen and L. Wang, Harnessing structural hierarchy to design stiff and lightweight phononic crystals, Extreme Mech. Lett. **9**, 91 (2016).

[45] C. Kittel, *Introduction to Solid State Physics* (Wiley, New York, 2005).

[46] W. Zhang, X. Lei, Z. Wang, D. Zheng, W. Y. Tam, C. T. Chan, and P. Sheng, Robust Photonic Band Gap from Tunable Scatterers, Phys. Rev. Lett. **84**, 2853 (2000).

[47] G. Wang, X. Wen, J. Wen, L. Shao, and Y. Liu, Two-Dimensional Locally Resonant Phononic Crystals with Binary Structures, Phys. Rev. Lett. **93**, 154302 (2004).

[48] N. Kaina, M. Fink, and G. Lerosey, Composite media mixing Bragg and local resonances for highly attenuating and broad bandgaps, Sci. Rep. **3**, 3240 (2013).

[49] P. Wang, J. Shim, and K. Bertoldi, Effects of geometric and material nonlinearities on tunable band gaps and

low-frequency directionality of phononic crystals, Phys. Rev. B **88**, 014304 (2013).

[50] T. Mullin, S. Deschanel, K. Bertoldi, and M. C. Boyce, Pattern Transformation Triggered by Deformation, Phys. Rev. Lett. **99**, 084301 (2007).

[51] L. Wang and K. Bertoldi, Mechanically tunable phononic band gaps in three-dimensional periodic elastomeric structures, Int. J. Solids Struct. **49**, 2881 (2012).

[52] C. Kane and T. Lubensky, Topological boundary modes in isostatic lattices, Nat. Phys. **10**, 39 (2014).

[53] Z.-G. Chen and Y. Wu, Tunable Topological Phononic Crystals, Phys. Rev. Applied **5**, 054021 (2016).

[54] E. Prodan and C. Prodan, Topological Phonon Modes and Their Role in Dynamic Instability of Microtubules, Phys. Rev. Lett. **103**, 248101 (2009).

[55] K. Bertoldi, V. Vitelli, J. Christensen, and M. van Hecke, Flexible mechanical metamaterials, Nat. Rev. Mater. **2**, 17066 (2017).

[56] Y. Achaoui, V. Laude, S. Benchabane, and A. Khelif, Local resonances in phononic crystals and in random arrangements of pillars on a surface, J. Appl. Phys. **114**, 104503 (2013).

[57] L. Brillouin, *Wave Propagation in Periodic Structures: Electric Filters and Crystal Lattices* (Courier Corporation, Mineola, New York, 2003).

[58] See Supplemental Material at http://link.aps.org/supplemental/10.1103/PhysRevApplied.9.044021 for details of the numerical simulations, theoretical formulation of the bounding frequencies, modeling and uncertainty analysis of geometric randomness, and supporting results of the 3D PnCs.

[59] J. R. Barber, *Elasticity* (Springer, New York, 1992).

[60] W. Thomson, *Theory of Vibration with Applications* (CRC Press, Boca Raton, FL, 1996).

[61] J.-C. Hsu and T.-T. Wu, Lamb waves in binary locally resonant phononic plates with two-dimensional lattices, Appl. Phys. Lett. **90**, 201904 (2007).

[62] H. H. Ku, Notes on the use of propagation of error formulas, J. Res. Natl. Bur. Stand. Sec. C: Eng. Inst. **70C**, 263 (1966).

[63] M. Danielsson, D. Parks, and M. Boyce, Three-dimensional micromechanical modeling of voided polymeric materials, J. Mech. Phys. Solids **50**, 351 (2002).

[64] L. Wang, M. C. Boyce, C. Y. Wen, and E. L. Thomas, Plastic dissipation mechanisms in periodic microframe-structured polymers, Adv. Funct. Mater. **19**, 1343 (2009).

[65] L. J. Gibson and M. F. Ashby, *Cellular Solids: Structure and Properties* (Cambridge University Press, Cambridge, England, 1999).

[66] B. Grünbaum and G. C. Shephard, *Tilings and Patterns* (Freeman, San Francisco, 1987).

[67] Y. Xia and G. M. Whitesides, Soft lithography, Annu. Rev. Mater. Sci. **28**, 153 (1998).

[68] J. Achenbach, *Wave Propagation in Elastic Solids* (Elsevier, New York, 2012), Vol. 16.

[69] L. D'Alessandro, E. Belloni, R. Ardito, A. Corigliano, and F. Braghin, Modeling and experimental verification of an ultra-wide bandgap in 3D phononic crystal, Appl. Phys. Lett. **109**, 221907 (2016).